

Ultrasound-Guided Optical Tomographic Imaging of Malignant and Benign Breast Lesions: Initial Clinical Results of 19 Cases¹

Quing Zhu*, Minming Huang*, NanGuang Chen*, Kristen Zarfos[†], Bipin Jagjivan[†], Mark Kane[†], Poornima Hedge[†] and Scott H. Kurtzman[†]

*Bioengineering Program, Electrical and Computer Engineering Department, University of Connecticut, Storrs, CT 06269-2157, USA; [†]University of Connecticut Health Center, Farmington, CT 06030, USA

Abstract

The diagnosis of solid benign and malignant tumors presents a unique challenge to all noninvasive imaging modalities. Ultrasound is used in conjunction with mammography to differentiate simple cysts from solid lesions. However, the overlapping appearances of benign and malignant lesions make ultrasound less useful in differentiating solid lesions, resulting in a large number of benign biopsies. Optical tomography using near-infrared diffused light has great potential for imaging functional parameters of 1) tumor hemoglobin concentration, 2) oxygen saturation, and 3) metabolism, as well as other tumor distinguishing characteristics. These parameters can differentiate benign from malignant lesions. However, optical tomography, when used alone, suffers from low spatial resolution and target localization uncertainty due to intensive light scattering. Our aim is to combine diffused light imaging with ultrasound in a novel way for the detection and diagnosis of solid lesions. Initial findings of two early-stage invasive carcinomas, one combined fibroadenoma and fibrocystic change with scattered foci of lobular neoplasia/lobular carcinoma *in situ*, and 16 benign lesions are reported in this paper. The invasive cancer cases reveal about two-fold greater total hemoglobin concentration (mean 119 μmol) than benign cases (mean 67 μmol), and suggest that the discrimination of benign and malignant breast lesions might be enhanced by this type of achievable optical quantification with ultrasound localization. Furthermore, the small invasive cancers are well localized and have wavelength-dependent appearance in optical absorption maps, whereas the benign lesions appear diffused and relatively wavelength-independent.

Neoplasia (2003) 5, 379–388

Keywords: breast cancer detection and diagnosis, optical tomography, ultrasound imaging, tumor angiogenesis, image reconstruction.

examinations [1]. When the criteria for a simple cyst are strictly adhered to, the accuracy of ultrasound is 96% to 100% [2]. Ultrasound specificity in breast cancer detection, however, is not high as a result of the overlapping characteristics of solid benign and malignant lesions [3,4]. The insufficient predictive value of ultrasound has prompted radiologists to recommend biopsies on most solid nodules, which result in a large number of biopsies yielding benign breast lesions. Currently, 70% to 80% percent of such biopsies yield benign findings [5]. In addition, the diagnostic accuracy of ultrasound depends largely on the experience of physicians.

Diffuse optical tomography in the near-infrared (NIR) is an emerging modality with potential applications in radiology and oncology [6–13]. Optical tomography with NIR light is made possible in a spectrum window that exists within tissues in the 700- to 900-nm NIR region, in which photon transport is dominated by scattering rather than absorption. Optical tomography offers several functional parameters to differentiate malignant cancers from benign lesions. It has been shown that breast cancers have higher blood volumes than nonmalignant tissues because of angiogenesis [14]. Tumor blood volume and microvascular density are parameters anatomically and functionally associated with tumor angiogenesis. If a single optical wavelength is used, optical absorption related to tumor angiogenesis and other normal blood vessels can be measured. If two or more optical wavelengths are used, both oxyhemoglobin (oxyHb) and deoxyhemoglobin (deoxyHb) concentrations can be measured simultaneously. However, optical tomography alone has not been widely used in clinical studies. The fundamental problem of intense light scattering remains, which makes the target localization difficult, especially for small lesions. In general, localization or imaging based on tomographic inverse scattering approaches suffers from low spatial resolution and location uncertainty, and the inversion problem

Introduction

Ultrasound imaging is a well-developed medical diagnostic tool that is used in conjunction with mammography for the differentiation of simple cysts from solid lesions in breast

Address all correspondence to: Prof. Quing Zhu, Bioengineering Program, Electrical Engineering Department, University of Connecticut, Storrs, CT 06269, USA. E-mail: zhu@engr.uconn.edu

¹We thank the following funding agents for their support: the DOD ARMY (DAMD17-00-1-0217, 17-01-1-0216), the Donaghue Foundation, and the National Institutes of Health (NIH; 1R01CA94044-01A1).

Received 31 March 2003; Revised 9 July 2003; Accepted 18 July 2003.

Copyright © 2003 Neoplasia Press, Inc. All rights reserved 1522-8002/03/\$25.00

is, in general, underdetermined and ill posed. The image reconstruction results depend on many parameters, such as the system signal-to-noise ratio, regularization schemes used in inversion, and so on.

Due to the above described deficiencies, literature data on optical tomography have been limited to feasibility studies or case reports [7–13]. However, these deficiencies can be overcome by a novel technique using a combination of NIR diffusive light and ultrasound [15–18]. The combined imager consists of a hand-held probe housing a commercial ultrasound probe and NIR source and detectors for coregistration. Ultrasound is used to scan suspicious lesions, whereas coregistered optical measurements are used to image and characterize the functional parameters of the lesions. With the *a priori* knowledge of lesion structure initially obtained by ultrasound, the tissue volume can be approximately segmented into a lesion region and a background region; optical reconstruction from the optical measurements can be performed by using finer imaging voxel size corresponding to the lesion region and coarse voxel size corresponding to the background region [18]. Consequently, the image reconstruction is well defined because the total number of imaging voxels with unknown optical properties is reduced significantly. In addition, the reconstruction is less sensitive to noise because the weight matrix is appropriately scaled for inversion, and convergence can be achieved within a small number of iterations.

In this paper, we report our initial clinical results of using the combined technique to image and characterize ultrasonically detected breast lesions. A total of 18 patients (19 cases) of invasive breast carcinomas (2 cases), combined fibroadenoma and fibrocystic changes with scattered foci of lobular neoplasia/lobular carcinoma *in situ* (noninvasive carcinoma; 1 case), juvenile atypical ductal hyperplasia (1 case), and fibroadenomas and fibrocystic changes (15 cases) are reported here. The diameters of these lesions are on the order of 1 cm. For the first time, we report high sensitivity of optical tomography in diagnosing early-stage invasive cancers and in differentiating them from small benign lesions. We also show a highly localized pattern of angiogenesis distribution of small invasive cancers. Our initial results are very encouraging and suggest that the discrimination of benign and malignant breast masses could be enhanced by this type of achievable optical quantification coupled with ultrasound localization.

Materials and Methods

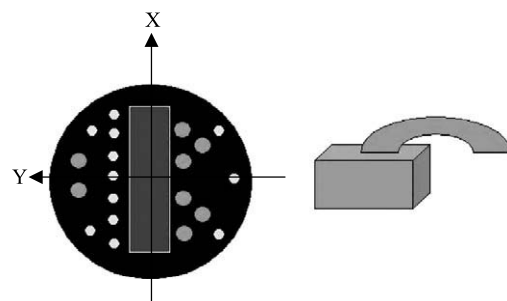
The major technical aspects of our combined imaging technique have been described in detail previously [16]. Briefly, the NIR system consists of 12 pairs of dual-wavelength (780 and 830 nm) laser diodes, which are used as light sources, and their outputs are amplitude-modulated at 140 MHz. For each source pair, the outputs from the two laser diodes at both wavelengths were coupled to the tissues through a 200- μ m optical fiber. On the receiver side, eight photomultiplier tubes (PMTs) were used to detect diffusely scattered light from the tissues, and eight optical fibers (3 mm in diameter)

were used to couple detected diffusive light from the tissues to the PMTs. The high-frequency radiofrequency (RF) signals were amplified and heterodyned to 20 kHz. The heterodyned signals were further amplified and band pass-filtered at 20 kHz. A reference signal of 20 kHz was also generated by directly mixing the detected RF signals with the RF signal generated from the oscillator. The reference signal was necessary for retrieving phase shifts. Eight detection signals and one reference were sampled and acquired into the PC simultaneously. The entire data acquisition took about 3 to 4 seconds, which was fast enough for acquiring data from patients.

A picture of our combined probe and imaging system used in the reported clinical studies is shown in Figure 1a, and the probe configuration and optical sensor distribution are shown in Figure 1b. Both amplitude and phase at each source–detector pair are obtained and the resulting total number of measurements is $12 \times 8 \times 2 = 192$. The combined probe is made of a black plastic plate 10 cm in diameter; therefore, a semi-infinite boundary condition can be used for NIR measurement geometry. The amplitudes and phases acquired at all source–detector pairs at the normal contralateral breast were used to calculate the



(a)



(b)

Figure 1. (a) Picture of the combined probe and frequency domain imager. (b) Sensor distribution of the combined probe. Smaller circles in (b) are optical source fibers and big circles are detector fibers. A commercial ultrasound probe is located at the center of the combined probe, and the optical source and detector fibers are distributed at the periphery of the ultrasound probe.

background absorption coefficient $\bar{\mu}_a$ and the reduced scattering coefficient $\bar{\mu}_s'$.

The details of our dual-mesh optical imaging reconstruction algorithm have been described in Ref. [18]. Briefly, the entire tissue volume is segmented based on initial coregistered ultrasound measurements into a lesion region L and a background region B . A modified Born approximation is used to relate the scattered field $U_{sd}(r_{su}, r_{dt}, \omega)$ measured at the source (s) and detector (d) pair i to absorption variations $\Delta\mu_a(r')$ in each volume element of two regions within the sample. The matrix form of image reconstruction is given by:

$$[U_{sd}]_{M \times I} = [W_L, W_B]_{M \times N} [M_L, M_B]_{N \times 1}^T$$

where W_L and W_B are weight matrices for lesion and background regions, respectively; and $[M_L] = [\int_{V_L} \Delta\mu_a(r') d^3r', \dots, \int_{V_L} \Delta\mu_a(r') d^3r']$ and $[M_B] = [\int_{V_B} \Delta\mu_a(r') d^3r', \dots, \int_{V_B} \Delta\mu_a(r') d^3r']$ are total absorption distributions of lesion and background regions, respectively. The weight matrices are calculated based on the background $\bar{\mu}_a$ and $\bar{\mu}_s'$ measurements obtained from the normal contralateral breast.

Instead of reconstructing the $\Delta\mu_a$ distribution directly, as is done in the standard Born approximation, the total absorption distribution M is reconstructed and the total is divided by different voxel sizes of lesions and background tissues to obtain the $\Delta\mu_a$ distribution. By choosing a finer grid for lesion and a coarse grid for background tissues, we can maintain the total number of voxels with unknown absorption on the same scale of the total measurements. As a result, the inverse problem is less underdetermined. In addition, because the lesion absorption coefficient is higher than that of background tissues, in general, the total absorption of the lesion over a smaller voxel is on the same scale as the total absorption of the background over a bigger voxel. Therefore, the matrix $[M_L, M_B]$ is appropriately scaled for inversion. In all experiments, a finer grid of $0.5 \times 0.5 \times 0.5$ (cm³) and a coarse grid of $1.5 \times 1.5 \times 1.5$ (cm³) were chosen for the lesion region and the background tissues, respectively. The total reconstruction volume was chosen to be $9 \times 9 \times 4$ cm³. The reconstruction is formulated as a least square problem and the unknown distribution M is iteratively calculated using the standard conjugate gradient method.

The perturbations for both wavelengths used to calculate absorption maps were normalized as $U_{sd}(r_{si}, r_{di}, \omega) = \frac{U_L(r_{si}, r_{di}, \omega) - U_N(r_{si}, r_{di}, \omega)}{U_N(r_{si}, r_{di}, \omega)} U_B(r_{si}, r_{di}, \omega)$, where $U_L(r_{si}, r_{di}, \omega)$ and $U_N(r_{si}, r_{di}, \omega)$ were optical measurements obtained at the lesion region and the normal region of the contralateral breast, and $U_B(r_{si}, r_{di}, \omega)$ was the calculated incident field using the measured background. This procedure cancels the unknown system gains associated with different sources and detectors as well as electronic channels.

The commercial one-dimensional (1-D) ultrasound probe acquires two-dimensional (2-D) ultrasound images in the x - z plane (z is the propagation direction) and the 2-D NIR probe provides three-dimensional (3-D) optical measurements for 3-D image reconstruction. Therefore, at each location, a 2-D ultrasound image is coregistered with a corresponding set of 3-D optical measurements in the x - z plane. However, if we

approximate a lesion as an ellipsoid, we are able to estimate its diameters from two orthogonal ultrasound images. The 3-D lesion center can be approximated from two orthogonal 2-D ultrasound images. However, two sources of error can affect accurate lesion location and volume estimation. First, the diameter measurements of large irregular lesions are inaccurate because lesion boundaries may not be well defined in ultrasound images. Second, the target boundaries seen by different modalities may be different due to different contrast mechanisms. To account for these errors, we use a lesion center estimated from the 2-D coregistered ultrasound image and use much larger diameters in both spatial dimensions than ultrasound-measured ones to highlight the lesion region for fine-mesh optical reconstruction. We have found from experiments that the abovementioned measurement inaccuracies have little effects on reconstructed optical properties as long as the lesion depth is measured correctly and the total number of unknown voxels is of the same order as the total number of measurements. The lesion depth z and the lesion boundaries in the z direction can be estimated reasonably well from 2-D coregistered ultrasound using normal tissue structure patterns.

Clinical studies were performed at the University of Connecticut Health Center (UCHC; Farmington, CT). The UCHC IRB committee approved the human subject protocol. Patients with palpable and nonpalpable masses that were visible on clinical ultrasound and who were scheduled for biopsy were enrolled as research subjects. These subjects were scanned with the combined probe, and ultrasound images and optical measurements were acquired at multiple locations including the lesion region scanned at two orthogonal positions, a normal region of the same breast if the breast was large, and a normal symmetric region of the contralateral breast also scanned at two orthogonal positions.

Results

Examples of Invasive Cancers

Figure 2a shows a gray scale ultrasound image of a nonpalpable lesion of a 55-year-old woman. The ultrasound showed a nodular mass with internal echoes and the lesion was considered suspicious. The estimated lesion diameter measured from two orthogonal ultrasound images was 8 mm. An ultrasound-guided core needle biopsy was recommended and the biopsy result revealed that the lesion was intraductal and infiltrating ductal carcinoma (nuclear grade II, histologic grade III). The cancer, once removed from the breast, measured 1 cm in greatest diameter, and was composed predominantly of invasive carcinoma (>95%), extending to surgical margins. Negative margins were achieved upon reexcision.

The average tissue background absorption coefficients $\bar{\mu}_a$ and the reduced scattering coefficients $\bar{\mu}_s'$ at 780 and 830 nm were measured as $\mu_a^{780} = 0.02$ cm⁻¹, $\mu_s'^{780} = 8.2$ cm⁻¹, $\mu_a^{830} = 0.04$ cm⁻¹, and $\mu_s'^{830} = 6.0$ cm⁻¹, respectively. The initial estimates of the lesion center and the

diameter from coregistered ultrasound were (0, 0.3, 2.3) cm and 8 mm. To account for errors in lesion geometry estimate and for differences in optical contrast, we used a 6-cm diameter in both x and y spatial dimensions at the center of (0, 0.3, 2.3) cm for fine-mesh optical reconstruction. The lesion diameter in depth is estimated as 1 cm by comparing the top and the bottom of lesion boundaries from normal tissue patterns. The white arrow arrays on the top and bottom of the lesion in Figure 2a point to normal tissue boundaries.

The optical absorption maps at both wavelengths are shown in Figure 2, *b* and *c*, respectively. In both Figure 2, *b* and *c*, the first slice is 0.7 cm deep into the breast tissue from the skin surface and the last slice is closer to the chest wall. The spacing of the slices is 0.5 cm. The horizontal and vertical axes of each slice are spatial x and y dimensions of 9 cm in size. The lesion is well resolved in slice 5 and has shown much larger spatial extension at 830 nm than that at 780 nm. The measured maximum absorption coefficients are $\mu_a^{780} = 0.24 \text{ cm}^{-1}$ and $\mu_a^{830} = 0.28 \text{ cm}^{-1}$, respectively, and the absorption maxima at both wavelengths are located at (0, 1.0, 2.3) cm, which is close to the lesion center measured by ultrasound.

By assuming that the major chromophores are oxygenated (oxyHb) and deoxygenated (deoxyHb) hemoglobin molecules in the wavelength range studied, we can estimate the distribution of total hemoglobin concentration as shown in Figure 2d. The extinction coefficients used for calculating oxyHb and deoxyHb concentrations were $\epsilon_{\text{Hb}}^{780} = 2.54$, $\epsilon_{\text{HbO}_2}^{780} = 1.70$, $\epsilon_{\text{Hb}}^{830} = 1.80$, $\epsilon_{\text{HbO}_2}^{830} = 2.42$, obtained from Ref. [19] in a natural logarithm scale with units of inverse millimoles times inverse centimeters. The measured maximum total hemoglobin concentration for lesions is 122 μmol , and the measured average background hemoglobin concentration is 14 μmol . The spatial extent of the lesion's angiogenesis is measured from the full width at half maximum (FWHM) of the total hemoglobin map and it is estimated to be 2.0 cm. This number is about two and half times larger than the 8 mm diameter measured by ultrasound and suggests that optical contrasts extend well beyond the cancer periphery due to angiogenesis.

Because our hand-held probe can be easily rotated or translated, we have acquired at least three coregistered ultrasound and NIR data sets at the lesion location for each patient and have reconstructed corresponding optical absorption maps as well as the total hemoglobin concentration distribution under the coregistered ultrasound guidance. The average maximum total hemoglobin concentration at the cancer region is 115 μmol ($\pm 27.6 \mu\text{mol}$) and the average background total hemoglobin concentration is 13 μmol ($\pm 1.5 \mu\text{mol}$). The large standard deviation at the cancer region is likely related to the probe compression at different spatial locations and elastic properties of the blood vessels in the cancer region.

Another example was obtained from a 56-year-old woman who had a solid mass with internal ultrasound echoes measuring 9 mm in size (Figure 3a). The lesion was considered suspicious, and ultrasound-guided core needle biopsy revealed that the lesion was *in situ* and

invasive ductal carcinoma (nuclear grade II, histologic grade II). The tumor, once removed from the breast, measured 1.5 cm in greatest diameter, and was composed predominantly of invasive carcinoma (>80%), extending to the inferior/anterior surgical margin. Negative inferior margin was achieved upon reexcision.

The average tissue background absorption coefficient $\bar{\mu}_a$ and the reduced scattering coefficient $\bar{\mu}'_s$ at 780 and 830 nm were measured as $\mu_a^{780} = 0.04 \text{ cm}^{-1}$, $\mu_s^{830} = 4.7 \text{ cm}^{-1}$, $\mu_a^{780} = 0.03 \text{ cm}^{-1}$, and $\mu_a^{830} = 5.8 \text{ cm}^{-1}$, respectively. The initial estimate of the lesion center and diameters from coregistered ultrasound were (0, 0.6, 1.9) cm and 9 mm, respectively. Again, we used a 6-cm diameter in both x and y spatial dimensions at the center of (0, 0.6, 1.9) for fine-mesh optical reconstruction. The optical absorption maps at both wavelengths are shown in Figure 3, *b* and *c*, respectively. In Figure 3, *b* and *c*, the first slice is 0.4 cm deep into the breast tissues from the skin surface and the last slice is closer to the chest wall. The spacing between the slices is 0.5 cm. This lesion is well resolved in slice #4 and has shown much larger spatial extension at 780 nm than that at 830 nm. The measured maximum absorption coefficients are $\mu_a^{780} = 0.29 \text{ cm}^{-1}$ and $\mu_a^{830} = 0.25 \text{ cm}^{-1}$, respectively. The absorption maxima at both wavelengths are located at (0, 1.0, 1.9000) cm, which is very close to the lesion center measured by ultrasound. The calculated maximum total hemoglobin concentration of the lesion is 128 μmol , and the background concentration is 24 μmol . The measured FWHM of the total hemoglobin map is 3.5 cm, which is more than three times larger than the 9 mm diameter measured by ultrasound and again suggests that optical contrasts extend well beyond the cancer periphery due to angiogenesis. The average maximum total hemoglobin concentration calculated from three NIR data sets is 123 μmol ($\pm 6.2 \mu\text{mol}$) and the average background hemoglobin concentration is 24 μmol ($\pm 0.5 \mu\text{mol}$). The variation of total hemoglobin concentrations acquired at slightly different spatial probe positions is much smaller than that in the previous case.

An Example of Combined Fibroadenoma and Fibrocystic Changes with Scattered Foci of Lobular Neoplasia/Lobular Carcinoma In Situ (Noninvasive Carcinoma)

This patient had a solid lesion measuring 1.1 cm in diameter as shown in Figure 4a ultrasound image. The lesion was diagnosed as having a benign appearance; however, the biopsy result revealed combined fibrocystic changes associated with microcalcifications and scattered foci of lobular neoplasia/lobular carcinoma *in situ* with pagetoid extension along ducts, but no invasive carcinoma. Also present was a fibroadenoma involved by lobular neoplasia.

The average background tissue absorption coefficients and reduced scattering coefficients at both wavelengths were measured as $\mu_a^{780} = 0.04 \text{ cm}^{-1}$, $\mu_s^{780} = 3.3 \text{ cm}^{-1}$, $\mu_a^{830} = 0.02 \text{ cm}^{-1}$, and $\mu_s^{830} = 3.5 \text{ cm}^{-1}$, respectively. The initial estimate of the lesion center and the diameter from ultrasound were (0, 0.9, 1.4) and 1.1 cm. The reconstructed absorption maps as well as total hemoglobin concentration distribution are shown in Figure 4, *b–d*, respectively. The

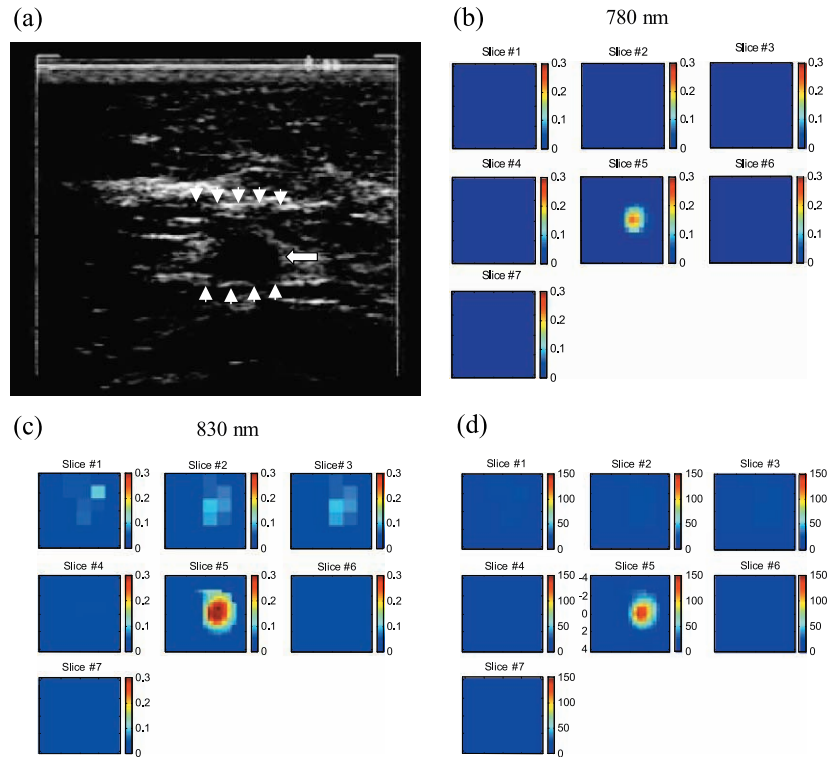


Figure 2. (a) shows a gray scale ultrasound image of a nonpalpable lesion of a 55-year-old woman. The lesion pointed by the arrow was located at the 4 o'clock position of the right breast measuring 8 mm in diameter. Ultrasound showed nodular mass with internal echoes and the lesion was considered suspicious. (b) and (c) are optical absorption maps at 780 and 830 nm, respectively. x and y axes are spatial dimensions of 9×9 cm. The slices starting from left to right correspond to absorption maps from 0.7 cm underneath the skin surface to the chest wall in 0.5-cm spacing. (d) is the total hemoglobin concentration and the vertical scale is in micromoles.

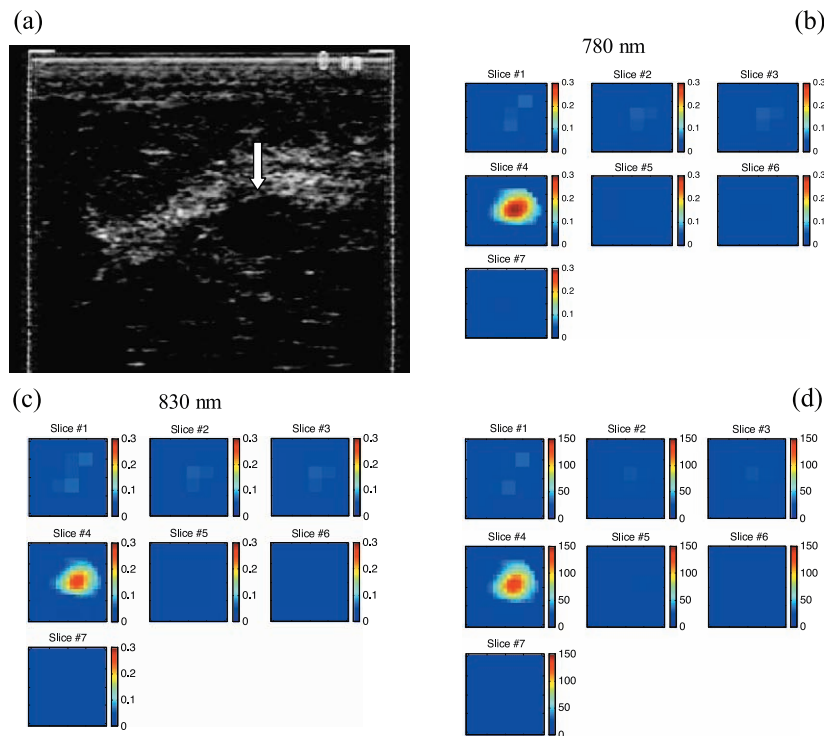


Figure 3. This example was obtained from a 56-year-old woman who had nonpalpable lesion located at the 10 o'clock position of the left breast. Ultrasound showed a solid mass (a) with internal echoes measuring 9 mm in size and the lesion was considered suspicious. (b) and (c) are optical absorption maps at 780 and 830 nm, respectively. The slices start from 0.4 cm underneath the skin surface to the chest wall in 0.5-cm spacing. (d) is the total hemoglobin concentration.

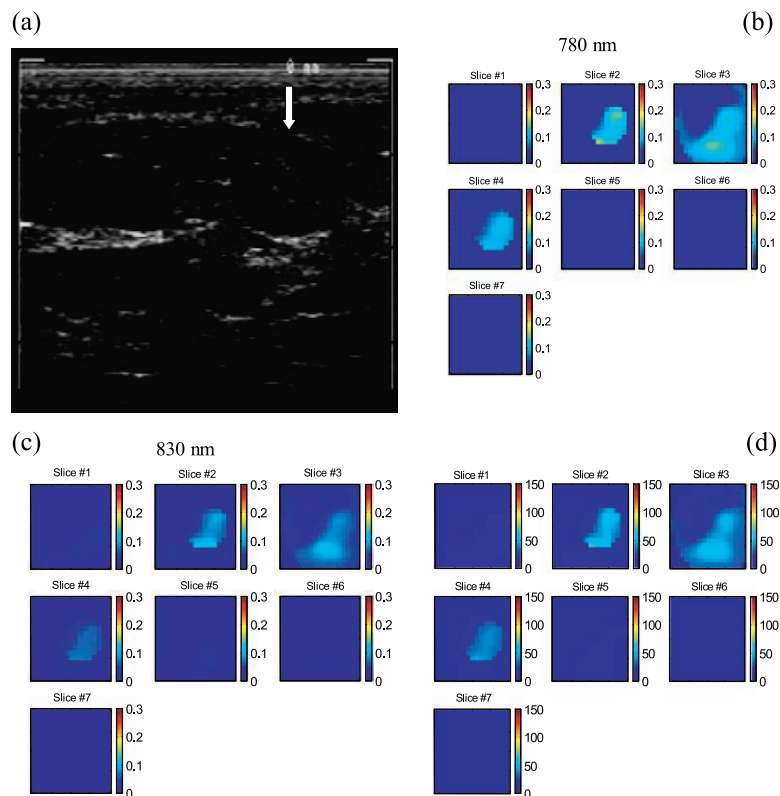


Figure 4. (a) shows a solid lesion at the 2 o'clock position measuring 1.1 cm in diameter in ultrasound image. The lesion was diagnosed as having benign appearance because of well-defined boundaries. Ultrasound-guided core biopsy revealed scattered foci of lobular neoplasia, carcinoma in situ but not invasive, and fibroadenoma and fibrocystic changes with associated microcalcifications. (b) and (c) are optical absorption maps at 780 and 830 nm, respectively. The slices start from 0.5 cm underneath the skin surface to the chest wall in 0.5-cm spacing. (d) is the total hemoglobin concentration.

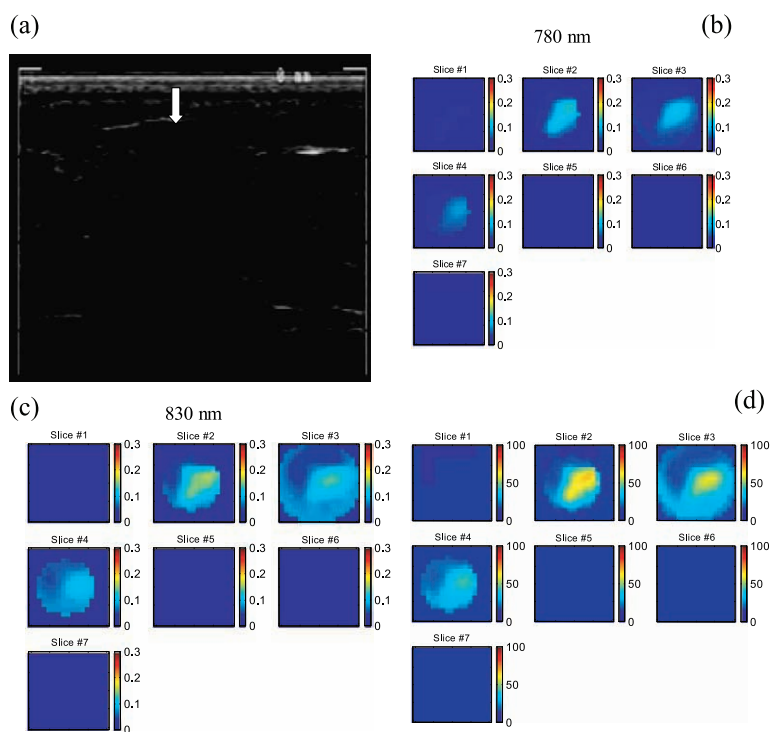


Figure 5. (a) shows an ultrasound image of a solid hypoechoic lesion located at 9 to 10 o'clock position of a 37-year-old woman's breast. The diagnosis was that the lesion could represent fibroadenoma; however, there was a chance that the lesion could be a carcinoma because of the irregular shape and posterior shadow seen by ultrasound. (b) and (c) are optical absorption maps at 780 and 830 nm, respectively. The slices start from 0.5 cm underneath the skin surface to the chest wall in 0.5-cm spacing. (d) is the total hemoglobin concentration.

measured maximum absorption coefficients are $\mu_a^{780} = 0.13 \text{ cm}^{-1}$ and $\mu_a^{830} = 0.09 \text{ cm}^{-1}$, respectively, which are about half of those measured in invasive cancer cases. In addition, the absorption coefficient distributions are diffused at both wavelengths and no resolvable or localized lesions are seen. The calculated maximum total hemoglobin concentration is $53 \text{ } \mu\text{mol}$, which is less than half of those in invasive cancer cases. The calculated background value is $13 \text{ } \mu\text{mol}$. The average maximum hemoglobin concentration calculated from four reconstructed NIR images at lesion location is $48 \text{ } \mu\text{mol}$ ($\pm 2.8 \text{ } \mu\text{mol}$) and the value for the background is $12 \text{ } \mu\text{mol}$ ($\pm 0.4 \text{ } \mu\text{mol}$). This example suggests that tumor vascularization may not be developed at the early noninvasive stage of combined fibrocystic change and neoplasia/carcinoma *in situ*.

Example of Fibroadenoma and Other Benign Lesions

Figure 5a shows an ultrasound image of a hypoechoic mass of a 37-year-old woman. The diagnosis was that the lesion likely was a fibroadenoma; however, there was concern that the lesion could be a carcinoma because of the irregular shape and the posterior shadowing seen by ultrasound. An ultrasound-guided core breast biopsy revealed that the lesion was simply a fibroadenoma.

Optical absorption maps are shown in Figure 5, *b* and *c*, as well as the total hemoglobin distribution in Figure 5*d*. Compared with the invasive cancer cases, the spatial distributions of the absorption coefficients as well as the total hemoglobin concentration are quite diffused, and a higher absorption region at 830 nm corresponds to lesion regions seen by ultrasound. The measured maximum lesion absorption coefficients at 780 and 830 nm are $\mu_a^{780} = 0.10 \text{ cm}^{-1}$ and $\mu_a^{830} = 0.12 \text{ cm}^{-1}$, respectively, and these values are less than half of those small invasive cancer cases. The calculated maximum total hemoglobin concentration is $52 \text{ } \mu\text{mol}$ and the background hemoglobin concentration is $14 \text{ } \mu\text{mol}$. The calculated average maximum total hemoglobin concentration from four NIR images acquired at lesion region is $59 \text{ } \mu\text{mol}$ ($\pm 5.1 \text{ } \mu\text{mol}$) and the average background is $16 \text{ } \mu\text{mol}$ ($\pm 1.0 \text{ } \mu\text{mol}$).

Table 1 lists all the measured parameters of the 19 cases [from left to right: biopsy result, lesion size measured by ultrasound in *x* and *z* dimensions (because lesions are small, the lesion size in *y* is similar to that measured in the *x* dimension), region of interest (ROI) used for fine-mesh NIR imaging, FWHM measured from NIR imaging, maximum absorption coefficients measured at both wavelengths, maximum and average total hemoglobin concentrations (the average is computed within FWHM)]. For the two invasive cancer cases, NIR parameters are given for two different ROIs and the results show that the choice of ROI has negligible effects on the absorption and hemoglobin measurements.

The statistics of maximum total hemoglobin concentration of three groups obtained from the 19 cases are shown in Figure 6. The benign group of fibroadenoma (15 cases) and hyperplasia (1 case) has an average of $67 \text{ } \mu\text{mol}$ (± 17.0

μmol), the combined fibroadenoma and fibrocystic change with noninvasive neoplasia/carcinoma *in situ* case has a maximum of $48 \text{ } \mu\text{mol}$, and the invasive cancer group of two cases has shown about two-fold greater average of $119 \text{ } \mu\text{mol}$ ($\pm 1.6 \text{ } \mu\text{mol}$). If average total hemoglobin concentration is used, the values are 46 (± 11.3), 30 , and 86 (± 2.12) μmol for the three corresponding groups, respectively. The malignant group also presents about two-fold greater average hemoglobin concentration than that of the benign group. The average sizes of lesions of the three groups measured by ultrasound are 1.05 (± 0.3), 1.1 , and 0.9 (± 0.07) cm, respectively. The lesion size is the geometric mean of diameters measured in *x* and *z* dimensions.

Because our study is in its early clinical trial stage, we do not intend to provide the sensitivity and specificity of the combined method due to the limited sample size available. However, our initial findings are very encouraging and suggest that early-stage small invasive cancers have much higher optical contrast than benign lesions and could be diagnosed with high specificity possibly due to tumor angiogenesis.

Discussion

As described earlier, due to intense light scattering, optical tomography alone has not been widely used in clinical studies. Data in the published literature have been limited to feasibility studies or case reports. Pogue et al. [9] reported pilot results of one invasive ductal carcinoma 1 cm in size and one benign fibroadenoma 3 cm in size. The reported maximum total hemoglobin concentrations were $68 \text{ } \mu\text{mol}$ for the cancer case and $55 \text{ } \mu\text{mol}$ for the benign case. Although the invasive cancer size reported by this group is comparable to ours, the system they used can only acquire NIR data from a ring area with optical sources and detectors deployed around the breast (2-D imager). Therefore, incomplete information could lead to smaller reconstructed absorption coefficients and total hemoglobin concentrations than those reported here using our 3-D NIR imager. In addition, an investigation with phantoms has shown that NIR alone, in general, reconstructs lower absorption coefficients and therefore lower total hemoglobin concentrations than true values [20]. This can be seen from two studies of the same data reported in Refs. [7,13]. Authors in Ref. [7] reported an average of $35 \text{ } \mu\text{mol}$ total hemoglobin concentration of a 2-cm ductal carcinoma *in situ* by using NIR measurements alone. After reprocessing the same NIR measurement data using an approximate lesion depth obtained from a separate ultrasound image, the authors reported that the calculated average total hemoglobin concentration was increased to $67 \text{ } \mu\text{mol}$ [13].

The reported small early-stage invasive cancers appear isolated and are well resolved from background tissues in optical absorption maps as well as in total hemoglobin distributions. However, the combined fibroadenoma and fibrocystic change with scattered foci of lobular neoplasia/lobular carcinoma *in situ* case showed no difference in optical absorption and hemoglobin concentration than those

Table 1. Measured Parameters of 19 Cases.

Reference Number	Biopsy Results	Lesion Size (Ultrasound) [cm]	ROI	FWHM (NIR) [cm]	Max μ_a [cm ⁻¹], 780 nm	Max μ_a [cm ⁻¹], 830 nm	Max Total Hb [μ M]	Average Total Hb [μ M]
13	Invasive cancer	0.9 × 0.6	6 × 6 × 1	3.5	0.28	0.24	123	87
			10 × 10 × 1	3.5	0.27	0.24	122	88
25	Invasive cancer	0.8 × 0.5	6 × 6 × 1	2.0	0.22	0.26	115	84
			10 × 10 × 1	2.1	0.22	0.26	115	84
32	Fibrocystic and lobular neoplasia/carcinoma	1.1 × 1.1	10 × 10 × 1.2	6.1	0.12	0.08	48	30
11	Fibroadenoma	1.2 × 0.8	8 × 8 × 1	4.9	0.11	0.10	49	37
8	Fibroadenoma	2.2 × 1.3	8 × 8 × 1.6	2.7	0.07	0.03	24	16
9	Fibroadenoma	0.9 × 0.7	8 × 8 × 1	4.9	0.15	0.18	77	52
7	Fibroadenoma and sclerosing adenosis with extensive calcification	1.0 × 0.6	10 × 10 × 1	3.8	0.16	0.11	59	41
17	Fibrocystic changes	0.6 × 0.7	10 × 10 × 1	5.8	0.16	0.16	76	53
20	Fibroadenoma	1.2 × 0.6	10 × 10 × 1	5.7	0.14	0.14	67	45
30	1: Fibrocystic change	1.7 × 1.1	8 × 8 × 1.3	4.0	0.10	0.15	59	39
30	2: Sclerosing adenosis and epithelial hyperplasia without atypical	1.4 × 1.2	8 × 8 × 1.3	4.0	0.15	0.23	88	57
22	Fibroadenoma	1.0*	10 × 10 × 1.5	3.7	0.15	0.15	72	46
36	Fibroadenoma	1.9 × 0.9	9 × 9 × 1	4.7	0.13	0.18	73	50
28	Fibroadenoma	1.9 × 1.1	9 × 9 × 1.3	4.2	0.14	0.16	71	45
33	Fibroadenoma	1.2 × 0.7	10 × 10 × 1	7.0	0.13	0.13	61	44
37	Fibroadenoma	0.8 × 0.6	8 × 8 × 1	6.0	0.16	0.18	80	53
35	Fibroadenoma	1.3 × 1.3	9 × 9 × 2	4.3	0.14	0.15	59	41
38	Hyalinized fibroadenoma	0.8 × 0.4	6 × 6 × 1	2.5	0.17	0.22	90	67
29	Atypical ductal hyperplasia	1.1 × 0.8	9 × 9 × 1	3.7	0.10	0.17	64	44

*See by X-ray.

obtained from fibroadenoma cases. This suggests that optical tomography may not be sensitive to early-stage mixed benign changes and noninvasive neoplasia/carcinoma *in situ* because tumor neovascularization has not been developed. This result is consistent with magnetic resonance imaging

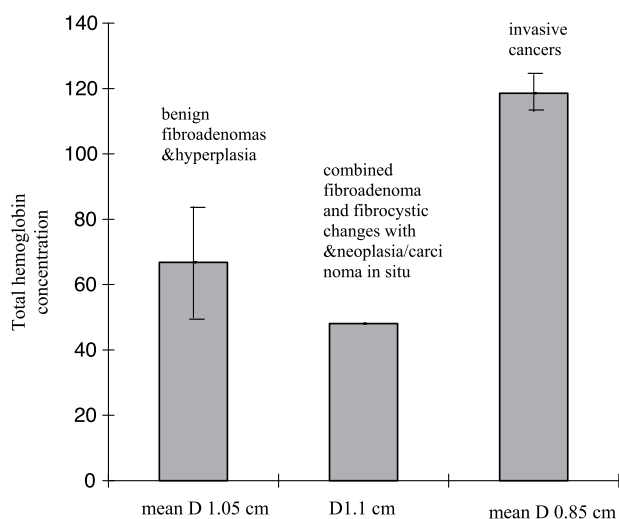


Figure 6. The average maximum total hemoglobin concentration obtained from benign fibroadenomas and hyperplasia, and combined fibroadenoma and fibrocystic change with neoplasia/carcinoma *in situ* (noninvasive) and invasive cancer groups are shown in bars. The standard deviations of three groups are also provided. The average sizes of lesions of the three groups are 1.05 (0.3), 1.1, and 0.9 (0.07) cm, respectively.

(MRI) findings on the low detection sensitivity of carcinoma *in situ* [21–23]. However, optical imaging may be a valuable tool for monitoring the development or transition of lesions from noninvasive to early invasive stage. Certainly, more cases are needed to validate the observations reported here. For larger cancers, highly heterogeneous wavelength-dependent optical absorption distributions and total hemoglobin distribution have been observed in four cases [18], and these distributions could provide valuable information for monitoring and assessing cancer therapy under treatment. Currently, we are pursuing research along this line and more cases will be reported in the future.

In principle, the distribution of oxygenation saturation can be estimated as $S = \text{oxyHb}/(\text{oxyHb} + \text{deoxyHb})$, with deoxyHb and oxyHb distributions calculated from absorption maps at the two wavelengths of 780 and 830 nm. However, because background tissues mainly consist of water and lipid and these two chromophores contribute to the total absorption estimate as well, we could not obtain reasonable background oxygenation saturation and compare it with lesion oxygenation saturation. Recently, we have improved our NIR system by adding another wavelength at 660 nm, which may allow us to accurately estimate the background oxygenation saturation and to compare it with lesion oxygenation saturation.

If we reconstruct the lesion area only, we could distribute partial perturbations caused by background to lesion and increase calculated lesion absorption and therefore hemoglobin concentration. However, with the dual-mesh scheme,

we reconstruct the entire imaging volume instead of the lesion area only, and distribute the perturbations to both lesion and background. We did phantom experiments using the dual-mesh scheme and obtained absorption coefficients, which were always within 10% of the true values depending on the phantom contrasts [24].

Two-dimensional ultrasound provides fine tissue layer structures in depth (z) direction (Figure 2, *arrow arrays*), and the 2-D ultrasound image is coregistered with optical data in z . Therefore, we only need to consider possible angiogenesis extensions in z and we have extended the lesions to the closest normal tissue lines in z . In spatial dimensions, we have some uncertainty in another dimension (y) based on 2-D x - z ultrasound image, and we need to extend the lesion region to a larger area to account for this as well as for possible angiogenesis extension.

The reported optical tomography study was used to image and characterize ultrasonically detected lesions. However, in one benign fibroadenoma case, the lesion was not visible in ultrasound but was seen by conventional X-ray mammogram. By knowing the approximate lesion region with respect to the nipple location from the patient's mammogram, we used a fine mesh for optical reconstruction in a larger region of $9 \times 9 \times 1.5 \text{ cm}^3$, and identified a possible lesion that showed slightly higher optical absorption than that of the background. We believe that optical tomography, assisted by conventional mammography and/or ultrasound localization, has potential as a screening tool to identify and characterize malignancy.

Our initial findings provide evidence that optical tomography, combined with ultrasound, could be used to differentiate early-stage small invasive breast cancers from benign lesions. Because of the limited sample size available, we are not able to provide sensitivity and specificity results in this paper. In addition, for the patients studied, four fibroadenoma cases and one intraductal hyperplasia were excluded from the statistics shown in Figure 6. The four fibroadenoma cases were scanned at the beginning of the study. One patient was scanned after core biopsy due to scheduling problem, and the possible blood distribution change due to biopsy procedure has to be considered. The other three young patients have small and dense breasts. For these three patients, the optical amplitude and phase data sets were highly scattered even in the normal contralateral breast. Therefore, no reliable background tissue absorption and scattering coefficients can be obtained. Three possible sources for these findings were identified. First, because these breasts were small and dense, the skin and probe contact was not always good. Second, a thick gel layer used for coupling the ultrasound transducer with the skin can serve as a light tunneling medium from sources to detectors. This portion of the light can saturate the detectors and give false readings. Caution was taken in the later studies by compressing the probe harder against the examined breast to ensure good probe-tissue contact, and by placing a very thin gel layer underneath the ultrasound transducer during scanning. The third source are tissue heterogeneities of the young dense breasts. However, by

carefully removing outliers from normal breast data, we could obtain reasonably good reference data for imaging. One patient with intraductal hyperplasia data was excluded from the study. This patient had a solid lesion located at the nipple area and the nipple had a very dark color. Four NIR image data sets obtained at the lesion area had the same artifacts and the artifact consistently showed up with very high absorptions at both wavelengths. When the lesion locations were changed in different images with different probe positions, the artifact location changed very little. A similar artifact showed up in the two reference data sets acquired in the contralateral normal breast. We do not know the exact source of this artifact because there was no report that this patient had problems at the contralateral breast. Care was taken in the later studies by acquiring at least four reference data sets at the normal symmetric region of the contralateral breast, as well as at normal regions of the same lesion breast. Reference data sets were always checked for normal background absorption changes before imaging the lesions.

Summary

Initial clinical results from the use of optical tomography combined with conventional ultrasound demonstrate that there is a huge optical contrast between early-stage invasive cancers and benign solid lesions due to angiogenesis. An average of $52 \mu\text{mol}$ difference was obtained between two small invasive cancers and a group of 16 benign solid lesions. In addition, the small invasive cancers were localized well in absorption maps and have shown wavelength-dependent absorption changes, whereas the benign lesions appeared more diffused in absorption maps and have shown relatively wavelength-independent absorption changes. The combined fibrocystic changes and noninvasive neoplasia/carcinoma *in situ* case did not show a significant difference in optical absorption and total hemoglobin concentration than those of benign lesions. This suggests that the angiogenesis may not be developed at the early noninvasive stage of the mixed benign changes and fibroadenoma with neoplasia/carcinoma *in situ*. However, optical tomography may have a potential role in monitoring the development and/or transition of cancers from the noninvasive to the invasive stage.

Our reported initial results are very encouraging and demonstrate that our unique approach, which combines optical tomography with ultrasound, has great potential to detect and characterize breast lesions.

Acknowledgements

The authors thank Ellen Oliver, surgical nurse of the Cancer Center of the UCHC, for her continuous efforts on patient scheduling. Q. Zhu expresses her sincere thanks to Prof. Britton Chance of the University of Pennsylvania for his continuous encouragement and support on combined imaging and valuable discussions on cancer biology. Graduate students Puyun Guo, Shikui Yan, and Daqing Piao are

acknowledged for their continuous help on the NIR system construction and improvement.

References

- [1] Stavros TA, Thickman D, and Rapp C (1995). Solid breast nodules: use of sonography to distinguish between benign and malignant lesions. *Radiology* **196**, 123–34.
- [2] Sickles EA (1998). Detection and diagnosis of breast cancer with mammography. *Perspect Radiol* **1**, 36–65.
- [3] Rahbar G, Sie AC, Hansen GC, Prince JS, Melany ML, Reynolds H, Jackson VP, Sayre JW, and Bassett LW (1999). Benign versus malignant solid breast masses: US differentiation. *Radiology* **213**, 889–94.
- [4] Jackson VP (1995). The current role of ultrasonography in breast imaging. *Radiol Clin North Am* **33**, 1161–170.
- [5] Sickles EA (1988). Detection and diagnosis of breast cancer with mammography. *Perspect Radiol* **1**, 36–65.
- [6] Yodh A, and Chance B (1995). Spectroscopy and imaging with diffusing light. *Phys Today* **48**, 34–40.
- [7] Tromberg B, Shah N, Lanning R, Cerussi A, Espinoza J, Pham T, Svaasand L, and Butler J (2000). Non-invasive *in vivo* characterization of breast tumors using photon migration spectroscopy. *Neoplasia* **2** (1:2), 26–40.
- [8] Franceschini MA, Moesta KT, Fantini S, Gaida G, Gratton E, Jess H, Seeber M, Schlag PM, and Kashke M (1997). Frequency-domain techniques enhance optical mammography: initial clinical results. *Proc Natl Acad Sci* **94**, 6468–473.
- [9] Pogue B, Poplack SP, McBride TO, Wells WA, Osterman K, Osterberg U, and Paulsen KD (2001). Quantitative hemoglobin tomography with diffuse near-infrared spectroscopy: pilot results in the breast. *Radiology* **218**, 261–66.
- [10] Dehghani H, Pogue B, Poplack SP, and Paulsen KD (2003). Multi-wavelength three-dimensional near-infrared tomography of the breast: initial simulation, phantom, and clinical results. *Appl Opt* **42** (1), 135–45.
- [11] Ntziachristos V, Yodh A, Schnall M, and Chance B (2000). Concurrent MRI and diffuse optical tomography of breast after indocyanine green enhancement. *Proc Natl Acad Sci* **97** (6), 2267–772.
- [12] Jiang H, Xu Y, Iftimia N, Eggert J, Klove K, Baron L, and Fajardo L (2001). Three-dimensional optical tomographic imaging of breast in a human subject. *IEEE Trans Med Imaging* **20** (12), 1334–340.
- [13] Jholboke M, Tromberg B, Li X, Shah N, Fishkin J, Kidney D, Butler J, Chance B, and Yodh A (2000). Three-dimensional diffuse optical mammography with ultrasound localization in human subject. *J Biomed Opt* **5** (2), 237–47.
- [14] Vaupel P, Kallinowski F, and Okunieff P (1989). Blood flow, oxygen and nutrient supply, and metabolic microenvironment of human tumors: a review. *Cancer Res* **49**, 6449–465.
- [15] Zhu Q, Durduran T, Holboke M, Ntziachristos V, and Yodh A (1999). Imager that combines near infrared diffusive light and ultrasound. *Opt Lett* **24** (15), 1050–1052.
- [16] Chen NG, Guo PY, Yan SK, Piao DQ, and Zhu Q (2001). Simultaneous near infrared diffusive light and ultrasound imaging. *Appl Opt* **40** (34), 6367–380.
- [17] Zhu Q, Conant E, and Chance B (2000). Optical imaging as an adjunct to sonograph in differentiating benign from malignant breast lesions. *J Biomed Opt* **5** (2), 229–36.
- [18] Zhu Q, Chen NG, and Kurtzman HS (2003). Imaging tumor angiogenesis by the use of combined near infrared diffusive light and ultrasound. *Opt Lett* **28** (5), 337–39.
- [19] Cope M (1991). PhD Dissertation University of College London.
- [20] Zhu Q, Chen NG, Piao DQ, Guo PY, and Ding XH (2001). Design of near infrared imaging probe with the assistance of ultrasound localization. *Appl Opt* **40** (19), 3288–303.
- [21] Gilles R, Zafrani B, Guinebreteiere JM, Meunier M, Lucidarme O, Tardivon AA, Rochard F, Vanel D, Neuenschwander S, and Arriagada R (1995). Ductal carcinoma *in situ*: MRI imaging–histopathologic correlation. *Radiology* **196**, 415–19.
- [22] Fischer U, Westerhof JP, Brinck U, Korabiowska M, Schauer A, and Grabbe E (1996). The ductal carcinoma *in situ* in contrast-enhanced dynamic MR mammography. *RoFo* **164**, 290–94.
- [23] Orel SG, Mendoca MH, Reynolds C, Schnall MD, Solin LJ, and Sullivan DC (1997). MR imaging of ductal carcinoma *in situ*. *Radiology* **202**, 413–20.
- [24] Huang MM, Chen NG, Yuan BH, and Zhu Q (2003). 3D simultaneous absorption and scattering coefficients reconstruction for the reflection geometry. In *Optical Tomography and Spectroscopy of Tissue V*. B Chance, RR Alfano, BJ Tromberg, M Tamura, EM Sevick-Muraca (Eds). SPIE, Bellingham, WA. Vol. **4955**, pp. 52–58.